Ab initio study of H, B, C, N, O, and self-interstitial atoms in hcp-Zr

Daegun You [a], Shraddha Ganorkar [a], Minsoo Joo [a], Donghyun Park [a], Sooran Kim [b], Keonwook Kang [c, **], Dongwoo Lee [a, *]

[a] School of Mechanical Engineering, Sungkyunkwan University, Suwon, Gyeonggi-do, South Korea
[b] Department of Physics Education, Kyungpook National University, Daegu, South Korea
[c] Department of Mechanical Engineering, Yonsei University, Seoul, South Korea

ARTICLE INFO

ABSTRACT

In this work, we investigate the stabilities of H, B, C, N, O, and Zr atoms at various interstitial sites in hcp-Zr using a first-principles theoretical approach. The formation energy of each interstitial atom at each site in the hcp crystal was determined, and the difference in the energy at different sites were considered as a static energy barrier to predict energetically favored diffusion pathways. Linear and non-linear prediction models for the interstitial formation energy were developed using readily accessible chemical and structural input parameters. We show that a simple linear model predicts the formation energies of the interstitial atoms with an R^2 of 97%.

1. Introduction

As an atom is placed into an interstitial site of a crystal, the energy of the system changes due to the interaction of the inserted atom with its neighboring host atoms, which depends on the chemical and structural properties of the system. The energy change is defined as the formation energy (E_f), which is a measure of the stability of the interstitial atom. Fundamental understanding of E_f of the interstitial atoms, such as H, B, C, N, O, and Zr located in interstitial sites of Zr crystal is essential to predict the thermal stability of Zr in various environments or to properly design the initial stage of the synthesis processes of Zr-based compounds that play vital roles in the industrial applications [1—8].

Although the experimental techniques such as nuclear reaction analysis and nano-calorimetry can be utilized to determine E_f of interstitial atoms [9—12], it is challenging to determine the value for low concentration as the energy change is too small to measure for most of the experimental tools. The ab initio simulation based on the density functional theory (DFT) provides a reasonable alternative for determining the formation energies of crystal systems [13]. Materials Project [14] and AFLOWLIB [15] are the databases in which formation energies of various systems determined by DFT calculations have been stored. Also, several models to predict E_f using big data and machine learning have steadily been studied [16—18]. However, formation energies and prediction models for various interstitial atoms of the hcp-Zr crystal, especially for low concentration are not readily available in previous literature.

In this work, we determine formation energies of H, B, C, N, O, and Zr-self interstitial atoms located at various interstitial sites including Bond-centered (BC), Crowdion (CD), Hexahedral (Hexa), Plane-centered (PC), Octahedral (Octa), and Tetrahedral (Tetra) in the host Zr crystal using ab initio simulations. The static energy barrier was computed from the formation energy to predict the preferred diffusion path of each interstitial atom. Three different models to predict E_f are proposed from linear regressions using readily accessible structural and chemical input parameters.

2. Methods

The first-principles calculations based on the density functional theory (DFT) were carried out using the Vienna Ab-initio simulation package (VASP) [19]. The projected-augmented-waves (PAW) [20] with the Perdew-Burke-Ernzerhof (PBE) [21] exchange-correlation potentials were adopted. For Zr, the valence states were treated using a $Zr(4s^24p^65s^24d^2)$ with PAW-PBE Zr_sv pseudopotential. $H(1s^1)$, $B(2s^22p^1)$, $C(2s^22p^2)$, $N(2s^22p^3)$, and $O(2s^22p^4)$ pseudopotentials were employed for H, B, C, N, and O of PAW-PBE series, respectively. The cut-off energy for plane waves was set to

* Corresponding author.
** Corresponding author.
E-mail addresses: kwkang75@yonsei.ac.kr (K. Kang), dongwoolee@skku.edu (D. Lee).

400 eV, and the forces converged to within 0.02 eV/Å when the lattice parameters and atomic positions were optimized. We used a 54-atom Zr supercell ($3 \times 3 \times 3$) and one impurity atom in each interstitial site for the calculations. For Brillouin zone sampling, $6 \times 6 \times 4$ k-point mesh in the Monkhorst–Pack scheme was employed for the simulations.

3. Results and discussion

Fig. 1 (a) and (b) show the crystal structure of α-Zr ($P6_3/mmc$, $a = b = 3.24$ Å, $c = 5.17$ Å [22]) and its various interstitial sites, including Bond-centered (BC), Crowdion (CD), Hexahedral (Hexa), Plane-centered (PC), Octahedral (Octa), and Tetrahedral (Tetra), considered in this study. Table 1 lists the position of each site. For the first principles calculations, we created structures by inserting an atom (*H, B, C, N, O, and Zr*) in each interstitial site of the supercell that contains 54 Zr atoms (Fig. 1 (b)). Total 36 structures were produced and relaxed by using the conditions described in method section. In this study, we only considered stable and metastable sites that do not exhibit significant distortion as compared with the initial structures [10,23]. E_f of interstitial atoms can be formulated by Refs. [9,10].

$$E_f = E_{total} - 54 \times E_{Zr} - 1 \times E_{interstitial} \qquad (1)$$

here, E_{total} is the total energy of the supercell that contains 54 *Zr* atoms and an interstitial atom, E_{Zr} is the energy/atom of the Zr supercell without any interstitial atoms, and $E_{interstitial}$ is the energy/atom at the equilibrium phase of each interstitial element. The values of $E_{interstitial}$ for *H, B, C, N,* and *O,* as well as *Zr,* were obtained from the *ab-initio* based online materials database, Materials Project [14]. The model numbers, $E_{interstitial}$, and space groups of *H, B, C, N,* and *O* are respectively, mp-24504 (-3.39eV, $P6_3/mmc$), mp-160 (-6.68eV, $R\bar{3}m$), mp-48 (-9.22eV, $P6_3/mmc$), mp-154 (-8.33eV, $P2_13$), and mp-12957 (-4.94eV, $C2/m$). Relaxation of a pure Zr supercell with 54 atoms was performed, and the space group, lattice parameter, and E_{Zr} were determined as $P6_3/mmc$, $a = b = 3.24$ Å, $c = 5.17$ Å, and -8.55eV, respectively.

Fig. 2 shows the calculated values of E_f for the relaxed host-interstitial systems of Zr-H, Zr-B, Zr-C, Zr-N, Zr-O and Zr-Zr with the interstitial sites of Octa, CD, BC, Hexa, PC, and Tetra. Tetra is found unstable for interstitial atoms of B, C, N, Zr as the inserted atoms sild to nearby Hexa sites during the relaxation process. Similar instability in the tetrahedral site is also known for various interstitial atoms in hcp-Ti [26,27]. Similarly, the crystal system containing self-interstitial in CD and oxygen in BC experience a significant distortion in the structure hence all these impurities and sites were excluded from Fig. 2. In Fig. 2, E_f of some systems are compared with previous studies and show good agreements for corresponding sites [9,10,22,24,25]. E_f of each system at each site is

Interstitial site	Position
Crowdion (CD)	(0.83 0.17 0.75)
Octahedral (Octa)	(0.33 0.67 0.25)
Bond-Centered (BC)	(0.67 0.83 0.50)
Hexahedral (Hexa)	(0.00 0.00 0.50)
Plane-Centered (PC)	(0.33 0.67 0.50)
Tetrahedral (Tetra)	(0.67 0.33 0.12)

tabulated in Table 2.

Among the systems considered in this study, the most stable system (lowest E_f) is the Zr-O system with E_f ranging from -5.44 to -3.95 eV. Next stable system is identified for the Zr-N system ($E_f = -3.61 \sim -0.014$ eV). E_f of the Zr-C, Zr-H, and Zr-B systems are within similar ranges ($E_f = -1.53–2.18$ eV). The highest E_f, indicating the least stable system, was determined for the self-interstitial atom, which can be attributed to the large size of the interstitial atom and the small difference in electronegativity between the interstitial and the host atoms [24]. Interestingly, E_f found to be minimum at Octa for most of the systems except for the Zr-H system, indicating that Octa is an energetically favorable site. For H, the E_f is minimum at Tetra by an energy difference of 0.061 eV compared with Octa, which is in good agreement with previous reports [22,25].

Because the Octa is the most energetically favorable site for the interstitial atoms of B, C, N, O, and Zr, one would expect diffusion paths for the systems as Octa-SP-Octa, where SP stands for the saddle point. Depending upon the relative position of SP that requires minimum energy cost with respect to the Octa site, a direction of preferable diffusion path can be determined [9,10,22,23,27]. In this regard, we ignored unstable saddle points that require high energy and severe distortion of the host lattice for the interstitial diffusion. Also, the energy difference between Octa and SP or static energy barrier E_{sb} can be taken as a measure of the diffusion energy barrier: $E_{sb} = E_f^{SP} - E_f^{Octa}$ [9,10,22,23,27]. Here, the superscripts of E_f indicate corresponding sites. We regard CD, BC, Hexa, and PC as potential SPs for the Octa-SP-Octa transition in Zr [23]. Fig. 3 (a) and (b) show E_{sb} and several possible diffusion paths: along the basal plane (Octa-CD-Octa) and through the c-axis (Octa-BC-Octa, Octa-Hexa-Octa and Octa-PC-Octa). The values in parentheses in Table 2 indicate E_{sb}.

We find that the most preferred diffusion path that has a minimum value E_{sb} shows a strong dependency on the type of impurity atoms: B interstitial prefers diffusion through the basal plane while C, N, O, and Zr interstitials prefer diffusion along c-axis. In detail, the Octa-CD-Octa (along the basal plane) path requires the lowest static energy barrier for B, which is consistent with the Nudged Elastic Band (NEB) calculation result on the interstitial diffusion of B in Zr
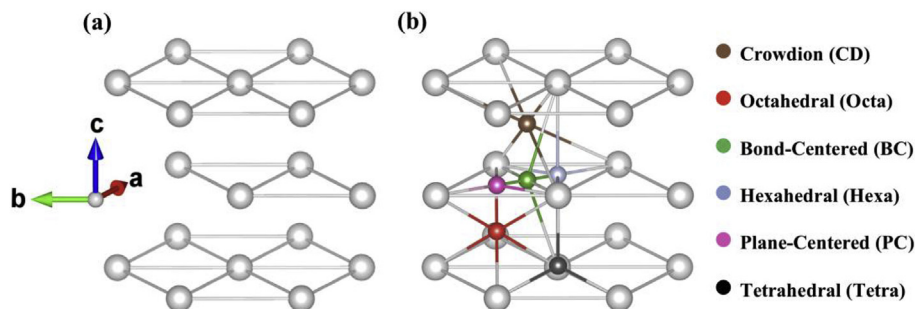

(a)   **(b)**

● Crowdion (CD)
● Octahedral (Octa)
● Bond-Centered (BC)
● Hexahedral (Hexa)
● Plane-Centered (PC)
● Tetrahedral (Tetra)

Fig. 1. (a) Crystal structure of hcp-Zr, (b) positions and local environments of various interstitial sites of Zr.
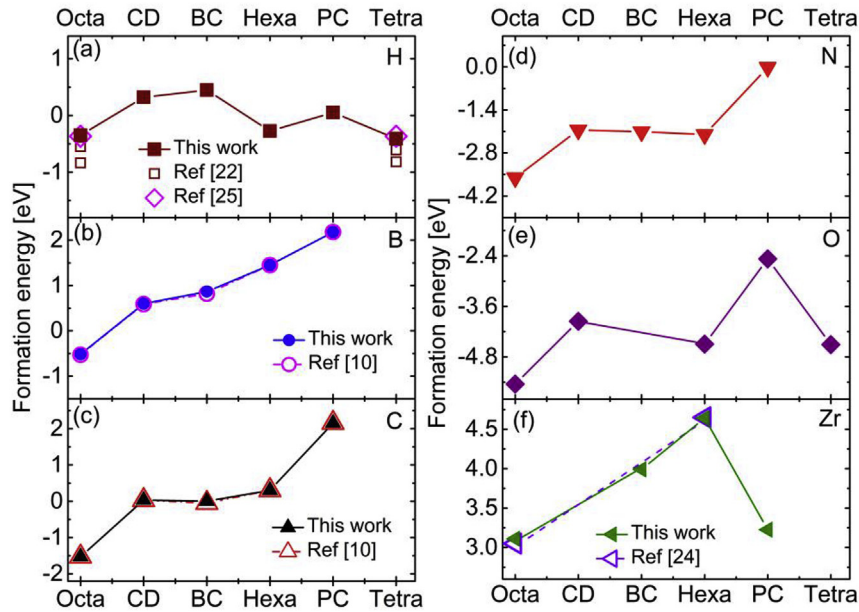
Fig. 2. The formation energies (E$_f$) of interstitial atoms at the various sites in the Zr crystal. The formation energies of several systems taken from Refs. [9,10,22,24,25] are compared.

Table 2
Formation energies of the interstitial atoms at various sites. The values in parentheses indicate the static energy barrier.

Interstitial site	E_{fH} (eV)	E_{fB} (eV)	E_{fC} (eV)	E_{fN} (eV)	E_{fO} (eV)	E_{fZr} (eV)
Octa	−0.35	−0.52	−1.53	−3.61	−5.44	3.11
CD	0.32	0.60 (1.12)	0.03 (1.56)	−2.05 (1.55)	−3.95 (1.49)	Unstable
BC	0.45	0.87 (1.38)	0.00 (1.53)	−2.11 (1.50)	Unstable	3.99 (0.88)
Hexa	−0.27	1.45 (1.97)	0.30 (1.83)	−2.20 (1.40)	−4.49 (0.95)	4.64 (1.53)
PC	0.051	2.18(2.70)	2.15(3.68)	−0.014 (3.60)	−2.47(2.97)	3.22(0.11)
Tetra	−0.41	Unstable	Unstable	Unstable	−4.51	Unstable

lattice [10]. The Octa-PC-Octa trajectory is expected to be the most preferred diffusion path for self intersitial (E_{sb} = 0.11 eV), while C takes a path of either the Octa-BC-Octa (along c-axis, E_{sb} = 1.53 eV) or the Octa-CD-Octa (through basal plane, E_{sb} = 1.56 eV). This result may indicate that the interstitial diffusion of C in Zr has an inter-penetrating network, meaning that C diffuses along both a and c axes, a similar behavior of O diffusion in Ti [27]. Unlike the C, B, and self-interstitial, N, and O have minimum values of E_{sb} for Octa-Hexa-Octa path and prefer diffusion along c-axis.

E_{sb} of H diffusion in Zr can be determined as $E_f^{SP} - E_f^{Tetra}$ as Tetra is the most stable interstitial site for the system (Table 2). H diffusion in Zr from Tetra to Octa then to another Tetra requires minimum E_{sb} along the basal plane. The Tetra-Octa interface (I$_{TO}$) is considered as SP for the diffusion, and E_f at I$_{TO}$ was calculated as −0.056 eV, making the Tetra-(I$_{TO}$)-Octa-(I$_{TO}$)-Tetra transition to have E_{sb} of 0.35 eV (Fig. 3 (c, d)). H diffusion along c-axis takes a path of Tetra-(I$_{TO}$)-Octa-Hexa-Octa-(I$_{TO}$)-Tetra with the minimum value of E_{sb}. The Octa-Hexa-Octa path requires 0.073 eV, resulting in the total value of E_{sb} of the diffusion through c-axis as 0.42 eV (Fig. 3 (c, d)). The calculated energy barrier for both directions agree very well with previous theoretical and experimental results [12,22].

Prediction models for E_f using easily accessible chemical and structural parameters as input parameters would be useful to understand the thermal stabilities of the interstitial atoms. To select proper input parameters, we refer to previous models that discuss the stability of alloys. Miedema's model is one of the successful semi-empirical models to estimate heats of formation of alloys [28]. Miedema et al. found that the formation energy of an alloy can be estimated using the electronegativity difference between the constituent atoms and difference in electron density at the boundary of the Wigner-Seitz cell, which can be determined by compressibility and molar volume. Miedema et al. also pointed out that coordination number would affect formation enthalpies of ordered alloys [29,30]. Also, according to the Hume-Rothery rules [31–34], atomic radii, electronegativities, valences, and crystal structures of solute and solution atoms affect the solubility. A recent work by W Ye et al. reported that electronegativity and ionic radii can be used as effective input parameters for predicting formation energies of garnets and perovskites [35].

Based on the input parameters of the above models and by taking into account the accessibilities of the parameters, we select electronegativity difference between the host atom and an interstitial atom (ΔEN) and the number of valence electrons (VE) of the interstitial atom as chemical input parameters. We also consider the average value of electronegativities between the interstitial and the host atoms (EN$_{avg}$) because together with ΔEN, this parameter can determine a type of bonding between elements according to the van Arkel diagram [36–39]. For structural input parameters, we use the coordination numbers (CN) of the interstitial sites. In addition, we use averaged value of the distance between the surfaces of an interstitial atom and its neighboring host atoms: $d_{surf} = |d_{avg} - (R_{Zr} + R_{imp})|$, where d_{avg} is the average distance between the center of an interstitial site and its vertices (d_i), R$_{Zr}$ and R$_{imp}$ are atomic radii of the host and an impurity atoms. Lastly, we consider the volume of the interstitial site (V) and the degree of symmetry of the interstitial sites which can be calculated as
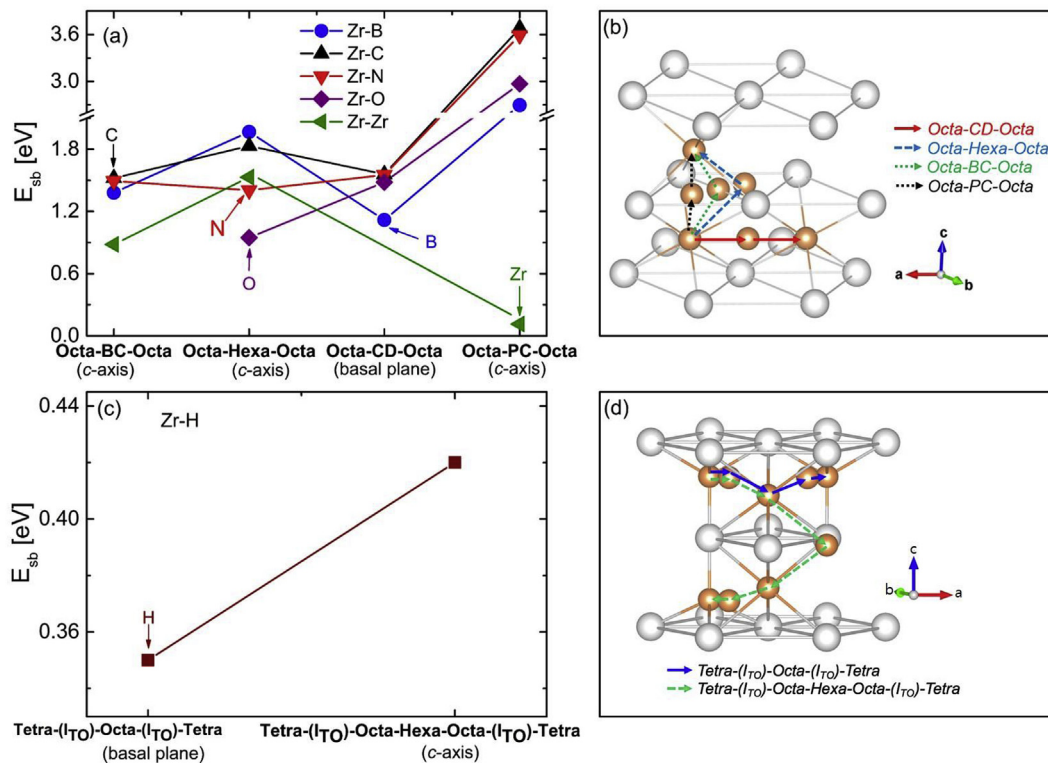
Fig. 3. Static energy barriers (E_{sb}) and diffusion pathways for B, C, N, O, and self-interstitial in Zr (a, b), and for H-Zr system (c, d). The arrows in (a, c) indicate most preferred diffusion pathway for each system.

$d_{sym} = 1 - d_{std}$, where d_{std} is the standard deviation of d_i. Selection of the structural parameters was also motivated by Lee et al. [10] who suggested that the interstitial formation energy is related to CN and the volume change upon insertion of the interstitial atom to a host crystal. Closer packing of atoms and more degree of symmetricity of an interstitial site will lead to less volume change after insertion of interstitial atoms. The values of chemical features and R_{imp} are listed in Table 3. In Table 4, the interstitial volume (V), d_{avg}, and d_i are represented. Note that all the chemical and structural parameters can be obtained without performing any *ab initio* simulations.

For the chosen seven input parameters (features) of ΔEN, EN_{avg}, VE, CN, d_{surf}, V, and d_{sym}, the method of feature scaling, general normalization (*min-max* normalization) [41–43] is applied. The normalization can be carried out using $x_i^* = \frac{x_i - x_{i(min)}}{x_{i(max)} - x_{i(min)}}$, where x_i^* is the normalized value of a feature x_i, while $x_{i(min)}$ and $x_{i(min)}$ are the minimum and maximum values of the feature, respectively. The normalized values of ΔEN and EN_{avg} were found to be the same, indicating that both features have an identical effect on E_f. Therefore, we remove ΔEN from the list of input parameters making the

Table 3
Electronegativity difference (ΔEN), average of electronegativity (EN_{avg}) in Pauling scale between the host and the interstitial atoms, the number of valence electrons (VE), and the radius of impurity (R_{imp}) [40] of the interstitial atom.

System	ΔEN	EN_{avg}	VE	R_{imp} (Å)
Zr-B	0.71	1.69	3	0.84
Zr-H	0.87	1.77	1	0.31
Zr-C	1.22	1.94	4	0.76
Zr-N	1.71	2.19	5	0.71
Zr-O	2.11	2.39	6	0.66
Zr-Zr	0	1.33	2	1.75

Table 4
Coordination number (CN), interstitial volume (V) and the distance between the center of the interstitial site and the vertices (d_i) of the pure Zr lattice. The #d_i (i = 1, 2, 3) is the number of equidistance bonds within each site.

Site	CN	V (Å^3)	d_1 (Å), (i = 1, 2, 3)						d_{sym} (Å)	d_{avg} (Å)
			d_1	#d_1	d_2	#d_2	d_3	#d_3		
Tetra	4	3.92	1.97	4	None	0	None	0	1	1.97
Hexa	5	7.83	1.87	3	2.59	2	None	0	0.61	2.16
Octa	6	15.66	2.27	6	None	0	None	0	1	2.27
CD	6	15.66	2.79	4	1.60	2	None	0	0.38	2.39
BC	6	15.66	2.75	2	1.62	2	2.81	2	0.40	2.39

total number of the feature as six.

A linear model is constructed in the form of $E_f^{lin,6} = \theta_0 + \theta_1 x_1 + \theta_2 x_2 + \ldots \theta_6 x_6$, where x_i are the input parameters and θ_i are the regression coefficients. The number in the superscript of the output parameter represents the number of features used in the model. The solution of the least square fit is given by $\Theta = (X^T X)^{-1} X^T E_f$, where $\Theta \in \mathbb{R}^{7 \times 1}$ and $X \in \mathbb{R}^{n \times 7}$, which is algebraically derived from the minimization of the error between E_f from the linear model and the DFT simulations, $\min \sum_k^n ((E_f)_k - (X\theta)_k)^2$. Here, X and Θ refer to the matrices that include all the values of the basis functions (1, x_1, x_2, …x_6) and the coefficients (θ_0, θ_1, …θ_6), respectively. In this analysis, we excluded the PC site due to the difficulty in defining geometric features such as CN and V. Depending on how to determine the cut-off bond length between an interstitial atom and its neighboring host atoms at the PC site, CN and V can either be 3 and 0 Å^3 or 9 and 31.33 Å^3. This characteristic makes Equation (2) for the PC site not applicable. For this reason, the total number of systems n for the analysis 24. The solution of the linear model is

given by:

$$E_f^{lin,6} = 14.34 - 7.68EN_{avg} + 0.13VE + 0.5d_{surf} - 2.16d_{sym}$$
$$+ 0.26CN - 0.085V \tag{2}$$

Fig. 4 (a) and (b) compare E_f determined by the DFT calculations and the values predicted by Equation (2). It is shown from the figure that the simple model describes the DFT results quite well: the coefficient of determination (R^2), root mean square error (RMSE), and mean absolute error (MAE) were determined as 0.97, 0.42 eV, and 0.34 eV respectively. Fig. 4 (a) uses a color code and a marker for the same interstitial atom, while Fig. 4 (b) uses different codes for different interstitial sites. As can be seen in Fig. 4 (a), the formation energy increases with decreasing value of EN_{avg}: lowest E_f for the Zr-O systems ($EN_{avg} = 2.39$) and highest E_f for the Zr-Zr systems ($EN_{avg} = 1.33$). Relatively close spacing of E_f are observed for the Zr-H, Zr-B, and Zr-C systems and their EN_{avg} are found to be located within a narrow range ($EN_{avg} = 1.69–1.94$). The results in Fig. 4 (b) indicate that E_f has less dependency on the type of interstitial site.

In addition to the linear model, we also consider non-linear prediction models with the exponential and power forms of $E_f^{xp,6} + C = \theta_0 e^{\theta_1 x_1} e^{\theta_2 x_2} ... e^{\theta_6 x_6}$ and $E_f^{pow,6} + C = \theta_0 x_1^{\theta_1} x_2^{\theta_2} ... x_6^{\theta_6}$. For both the models, we use $E_f + C$ as the output parameter because the exponential and the power equations cannot describe a sign change. The constant C is determined as 10 such that the all the output values ($E_f + C$) are positive. The non-linear equations can be linearized by taking their logarithms, allowing linear regression: $ln(E_f + C) = ln\theta_0 + \theta_1 x_1 + \theta_2 x_2 + \cdots + \theta_6 x_6$ and $ln(E_f + C) = ln\theta_0 + \theta_1 \ln x_1 + \theta_2 \ln x_2 + \cdots \theta_6 \ln x_6$. The regressions result in the following expressions:

$$E_f^{xp,\ 6} = 60.04e^{-0.97EN_{avg}} * e^{0.013VE} * e^{-0.096d_{surf}} * e^{-0.25d_{sym}} *$$
$$e^{0.049CN} * e^{-0.013V} - 10 \tag{3}$$

and

$$E_f^{pow,\ 6} = 2.01EN_{avg}^{-1.56} * VE^{-0.014} * d_{surf}^{-0.021} * d_{sym}^{-0.17} * CN^{2.45} * V^{-0.74}$$
$$- 10 \tag{4}$$

Fig. 4(c–f) compare E_f from the non-linear prediction models with the values determined from the DFT calculations. The model with the exponential form shows a reasonable agreement with the DFT results ($R^2 = 0.95$, RMSE = 0.61 eV, MAE = 0.49 eV), while the power model shows a less accuracy ($R^2 = 0.92$, RMSE = 0.75 eV, MAE = 0.61 eV). Nevertheless, the linear model in Equation (2) shows better performance to predict E_f as compared with the non-linear models.

The Pearson correlation coefficient (r_i) is a measure of the linear correlation between the input parameters and output parameters in a model. By determining r_i of an input parameter x_i, it is possible to determine the relative importance of the features [16,44].:

$$r_i = \frac{\sum_{k=1}^n (x_{i,\ k} - \overline{x}_i)\left(\left(E_f\right)_k - \overline{E_f}\right)}{\sqrt{\sum_{k=1}^n (x_{i,\ k} - \overline{x}_i)^2}\sqrt{\sum_{k=1}^n \left(\left(E_f\right)_k - \overline{E_f}\right)^2}} \tag{5}$$

here, x_i ($i = 1~6$) represents each feature (EN_{avg}, CN, V, d_{surf}, d_{sym}, and VE). The subscript k stands for each dataset of the total $n = 24$ systems. Note that the upper bar shows the average. The value of r_i ranges from -1 or 1. As r_i is closer to $|1|$, the corresponding feature
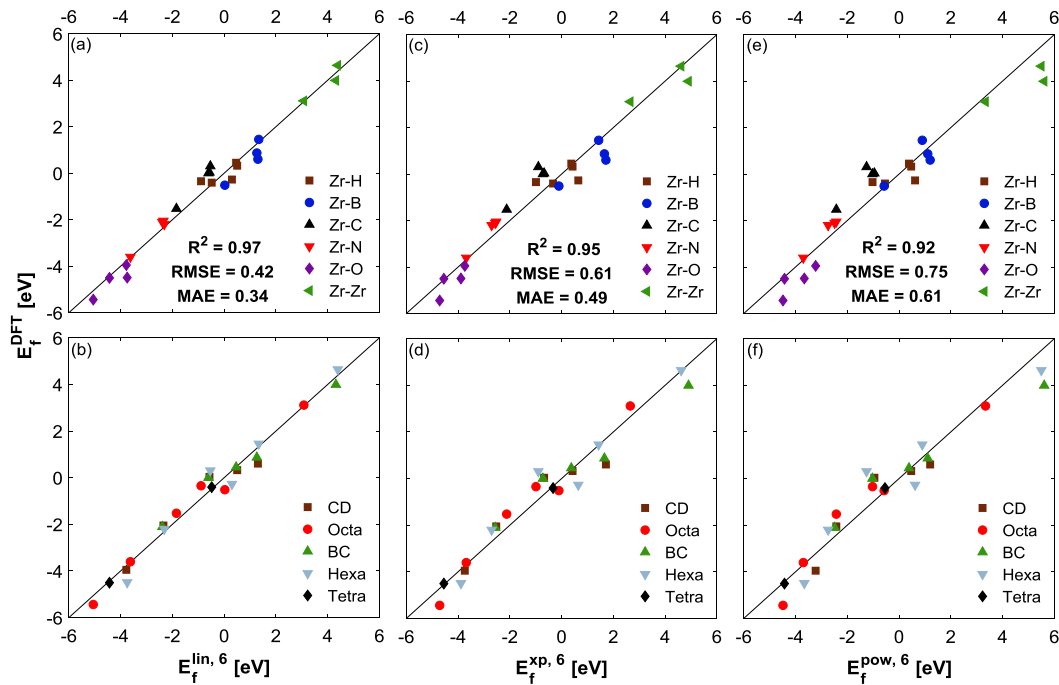

Fig. 4. Comparison of E_f from the prediction models and the DFT calculations: (a, b) the linear model, (c,d) th exponential model, and (e,f) the power model. The upper panels (a, c, e) show the result using a color code for the same interstitial atom and the bottom panel (b, d, f) use the same color and a marker for the same interstitial sites. (For interpretation of the references to color in this figure legend, the reader is referred to the Web version of this article.)
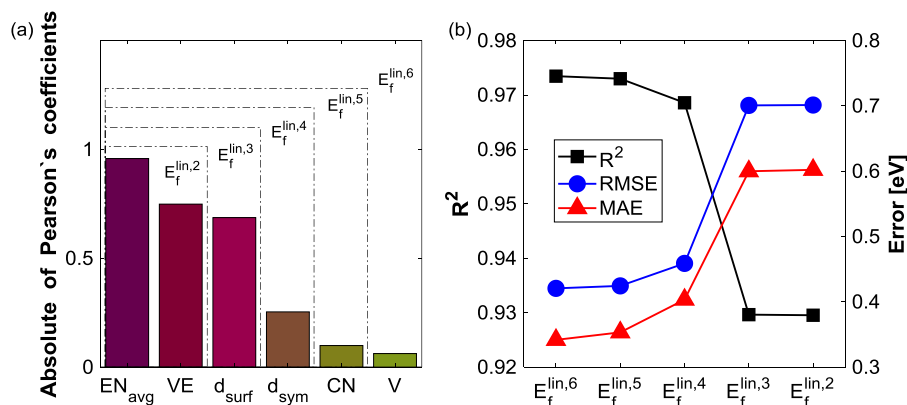
Fig. 5. (a) Pearson's correlation coefficient of each feature. Features used for different linear models are indicated by dotted box. (b) R^2, RMSE, and MAE of the linear models with various number of features.

has a stronger linear correlation with the output parameter, E_f. Fig. 5 (a) shows r_i of each feature. It is evident from the figure that EN_{avg} has the strongest linear relationship with E_f, followed by VE and d_{surf}. d_{sym}, CN, and V showed relatively weaker correlations with E_f. Note that the chemical input parameters have stronger relationships with E_f than the structural parameters do.

The linear model in Equation (2) can further be simplified: linear regressions were carried out using only two to five features, by removing weakly correlated input parameters based on the Pearson's correlation coefficients. The simplified linear models are as follows:

$$E_f^{lin,\,5} = 16.49 - 7.70EN_{avg} + 0.13VE + 0.53d_{surf} - 2.24d_{sym}$$
$$- 0.30CN \tag{6}$$

$$E_f^{lin,\,4} = 13.74 - 7.12EN_{avg} + 0.064VE + 0.81d_{surf} - 2.10d_{sym} \tag{7}$$

$$E_f^{lin,\,3} = 14.38 - 8.29EN_{avg} + 0.19VE + 0.13d_{surf} \tag{8}$$

$$E_f^{lin,\,2} = 14.38 - 8.47EN_{avg} + 0.21VE \tag{9}$$

Fig. 5 (b) displays R^2, RMSE, and MAE of the linear models with different numbers of features (Equations (2) and (6)–(9)). Reduction of the number of features to four does not sacrifice the accuracy significantly. The linear model with four key features of EN_{avg}, VE, d_{surf}, and d_{sym} still shows a high accuracy with R^2 of 0.97. However, R^2 of the model with three features drops suddenly to 0.93. This value is not very different from R^2 of the model with only two chemical features of EN_{avg} and VE. Note that the proposed models can only be applicable for the CD, Octa, BC, Tetra, and Hexa sites of Zr with high accuracy. More sophisticated models with machine learning techniques and careful selection of features may allow the prediction of the interstitial formation energies of broader range of interstitial-host atom systems.

4. Conclusion

In conclusion, the formation energies of interstitial atoms (H, B, C, N, O, and *self-interstitial*) at various interstitial sites of *hcp-Zr* have been investigated by using *ab initio* simulations. The static energy barrier was calculated to predict the energy barrier of each

interstitial diffusion and to identify the preferred diffusion path. Linear and non-linear prediction models using chemical and structural input parameters were proposed to describe the interstitial formation energies at CD, Octa, BC, Tetra, and Hexa sites. A linear model with four features showed a high accuracy ($R^2 = 97\%$) while non-linear power and exponential models have relatively lower accuracies. It was revealed that the key input parameters to describe E_f are the electronegativities of the constituent atoms, valence electrons, the distance between the host-interstitial pair, and the symmetricity of the interstitial sites. A similar behavior is expected to be found for other interstitial-hcp crystal systems, and the approach introduced in this work can be used to develop a model to predict the formation energies.

References

[1] P.W. Bickel, T.G. Berlincourt, Electrical properties of hydrides and deuterides of zirconium, Phys. Rev. B 2 (12) (1970) 4807–4813.
[2] L. Holliger, A. Legris, R. Besson, Hexagonal-based ordered phases in H-Zr, Phys. Rev. B 80 (9) (2009), 094111.
[3] C.R. Wang, J.M. Yang, W. Hoffman, Thermal stability of refractory carbide/boride composites, Mater. Chem. Phys. 74 (3) (2002) 272–281.
[4] R.J. Nicholls, N. Ni, S. Lozano-Perez, A. London, D.W. McComb, P.D. Nellist, C.R.M. Grovenor, C.J. Pickard, J.R. Yates, Crystal structure of the ZrO phase at zirconium/zirconium oxide interfaces, Adv. Eng. Mater. 17 (2) (2014) 211–215.
[5] W. Qin, C. Nam, H.L. Li, J.A. Szpunar, Tetragonal phase stability in ZrO2 film formed on zirconium alloys and its effects on corrosion resistance, Acta Mater. 55 (5) (2007) 1695–1701.
[6] X. Li, J. Shi, G. Zhang, H. Zhang, Q. Guo, L. Liu, Effect of ZrB2 on the ablation properties of carbon composites, Mater. Lett. 60 (7) (2006) 892–896.
[7] A. Choeysuppaket, N. Witit-Anun, S. Chaiyakun, Characterization of ZrN thin films deposited by reactive DC magnetron sputtering, Adv. Mater. Res. 770 (2013) 350–353.
[8] S.K. Nayak, C.J. Hung, V. Sharma, S.P. Alpay, A.M. Dongare, W.J. Brindley, R.J. Hebert, Insight into point defects and impurities in titanium from first principles, npj Comput. Mater. 4 (1) (2018) 11.
[9] D. Lee, G.D. Sim, K. Zhao, J.J. Vlassak, Kinetic role of carbon in solid-state synthesis of zirconium diboride using nanolaminates: nanocalorimetry experiments and first-principles calculations, Nano Lett. 15 (12) (2015) 8266–8270.
[10] D. Lee, J.J. Vlassak, K. Zhao, First-principles theoretical studies and nanocalorimetry experiments on solid-state alloying of Zr-B, Nano Lett. 15 (10) (2015) 6553–6558.
[11] E. Perim, D. Lee, Y. Liu, C. Toher, P. Gong, Y. Li, W.N. Simmons, O. Levy, J.J. Vlassak, J. Schroers, S. Curtarolo, Spectral descriptors for bulk metallic glasses based on the thermodynamics of competing crystalline phases, Nat.

Commun. 7 (2016) 12315.

[12] C.S. Zhang, B. Li, P.R. Norton, The study of hydrogen segregation on Zr(0001) and Zr(1010) surfaces by static secondary ion mass spectroscopy, work function, Auger electron spectroscopy and nuclear reaction analysis, J. Alloys. Compd. 231 (1) (1995) 354—363.

[13] Y. Zeng, Q. Li, K. Bai, Prediction of interstitial diffusion activation energies of nitrogen, oxygen, boron and carbon in bcc, fcc, and hcp metals using machine learning, Comput. Mater. Sci. 144 (2018) 232—247.

[14] A. Jain, S.P. Ong, G. Hautier, W. Chen, W.D. Richards, S. Dacek, S. Cholia, D. Gunter, D. Skinner, G. Ceder, K.A. Persson, Commentary: the Materials Project: a materials genome approach to accelerating materials innovation, Apl. Mater. 1 (1) (2013), 011002.

[15] S. Curtarolo, W. Setyawan, S. Wang, J. Xue, K. Yang, R.H. Taylor, L.J. Nelson, G.L.W. Hart, S. Sanvito, M. Buongiorno-Nardelli, N. Mingo, O. Levy, AFLOWL-IB.ORG, A distributed materials properties repository from high-throughput ab initio calculations, Comput. Mater. Sci. 58 (2012) 227—235.

[16] S. Ubaru, A. Miedlar, Y. Saad, J. Chelikowsky, Formation enthalpies for transition metal alloys using machine learning, Phys. Rev. B 95 (21) (2017), 214102.

[17] F. Faber, A. Lindmaa, O.A. von Lilienfeld, R. Armiento, Crystal structure representations for machine learning models of formation energies, Int. J. Quantum Chem. 115 (16) (2015) 1094—1101.

[18] F.A. Faber, A. Lindmaa, O.A. von Lilienfeld, R. Armiento, Machine learning energies of 2 million elpasolite (ABC_2D_6) crystals, Phys. Rev. Lett. 117 (13) (2016), 135502.

[19] G. Kresse, J. Furthmüller, Efficient iterative schemes for ab initio total-energy calculations using a plane-wave basis set, Phys. Rev. B 54 (16) (1996) 11169—11186.

[20] G. Kresse, D. Joubert, From ultrasoft pseudopotentials to the projector augmented-wave method, Phys. Rev. B 59 (3) (1999) 1758—1775.

[21] J.P. Perdew, K. Burke, M. Ernzerhof, Generalized gradient approximation made simple, Phys. Rev. Lett. 77 (18) (1996) 3865—3868.

[22] C. Domain, R. Besson, A. Legris, Atomic-scale Ab-initio study of the Zr-H system: I. Bulk properties, Acta Mater. 50 (13) (2002) 3513—3526.

[23] D. Lee, J.J. Vlassak, K. Zhao, First-principles analysis on the catalytic role of additives in low-temperature synthesis of transition metal diborides using nanolaminates, ACS Appl. Mater. Interfaces 8 (17) (2016) 10995—11000.

[24] Q. Peng, W. Ji, H. Huang, S. De, Stability of self-interstitial atoms in hcp-Zr, J. Nucl. Mater. 429 (1) (2012) 233—236.

[25] Y. Zhang, C. Jiang, X. Bai, Anisotropic hydrogen diffusion in α-Zr and Zircaloy predicted by accelerated kinetic Monte Carlo simulations, Sci. Rep. 7 (2017) 41033.

[26] R.G. Hennig, D.R. Trinkle, J. Bouchet, S.G. Srinivasan, R.C. Albers, J.W. Wilkins,

[27] H.H. Wu, D.R. Trinkle, Direct diffusion through interpenetrating networks: oxygen in titanium, Phys. Rev. Lett. 107 (4) (2011), 045504.

[28] A.R. Miedema, R. Boom, F.R. De Boer, On the heat of formation of solid alloys, J. Less Common Met. 41 (2) (1975) 283—298.

[29] A.R. Miedema, Simple model for alloys, Philips Tech. Rev. 33 (6) (1973) 149—160.

[30] A.R. Miedema, F.R.d. Boer, P.F.d. Chatel, Empirical description of the role of electronegativity in alloy formation, J. Phys. F Met. Phys. 3 (8) (1973) 1558.

[31] L.S. Darken, R.W. Gurry, Physical Chemistry of Metals (Metallurgy and Metallurgical Engineering Series), McGraw-Hill, New York, 1953.

[32] T. Massalski, Structure and stability of alloys, in: R.W. Cahn, P. Haasen (Eds.), Physical Metallurgy, 1996, pp. 135—204. North-Holland.

[33] U. Mizutani, Hume-Rothery rules for structurally complex alloy phases, MRS Bull. 37 (2) (2012) 169.

[34] W.H. Rothery, Researches on the nature, properties, and conditions of formation of intermetallic compounds, with special reference to certain compounds of tin-IV, J. Inst. Met. 35 (1926) 295—354.

[35] W. Ye, C. Chen, Z. Wang, I.-H. Chu, S.P. Ong, Deep neural networks for accurate predictions of crystal stability, Nat. Commun. 9 (1) (2018) 3800.

[36] L.C. Allen, Electronegativity is the average one-electron energy of the valence-shell electrons in ground-state free atoms, J. Am. Chem. Soc. 111 (25) (1989) 9003—9014.

[37] L.C. Allen, J.F. Capitani, G.A. Kolks, G.D. Sproul, Van Arkel—Ketelaar triangles, J. Mol. Struct. 300 (1993) 647—655.

[38] A.E.V. Arkel, Molecules and Crystals in Inorganic Chemistry, Interscience Publishers, New York, NY, USA, 1956.

[39] J.A.A. Ketelaar, Chemical Constitution : an Introduction to the Theory of the Chemical Bond, 2 ed., Elsevier, New York, NY, USA, 1958.

[40] B. Cordero, V. Gómez, A.E. Platero-Prats, M. Revés, J. Echeverría, E. Cremades, F. Barragán, S. Alvarez, Covalent radii revisited, Dalton Trans. 21 (2008) 2832—2838.

[41] C.C. Aggarwal, Data Preparation, Data Mining: the Textbook, Springer, 2015, p. 37.

[42] K. Doherty, R. Adams, N. Davey, Non-Euclidean norms and data normalisation, in: Proceedings European Symposium on Artificial Neural Networks Bruges (Belgium), 2004, pp. 181—186.

[43] M.M. Suarez-Alvarez, D.-T. Pham, M.Y. Prostov, Y.I. Prostov, Statistical approach to normalization of feature vectors and clustering of mixed datasets, Proc. R. Soc. A Math. Phys. Eng. Sci. 468 (2145) (2012) 2630—2651.

[44] G. Pilania, C. Wang, X. Jiang, S. Rajasekaran, R. Ramprasad, Accelerating materials property predictions using machine learning, Sci. Rep. 3 (2013) 2810.